Ciliary length regulation by intraflagellar transport in zebrafish

Yi Sun[1,5], Zhe Chen[1,4,5], Minjun Jin[1,2], Haibo Xie[1,2], Chengtian Zhao[1,2,3]

[1]Key Laboratory of Evolution and Marine Biodiversity (MOE) and Institute of Evolution and Marine Biodiversity, Ocean University of China, Qingdao, 266003, China

[2]Fang Zongxi Center for Marine Evo Devo, College of Marine Life Sciences, Ocean University of China, Qingdao, 266003, China

[3]Laboratory for Marine Biology and Biotechnology, Qingdao National Laboratory for Marine Science and Technology, Qingdao, 266003, China

[4]Tsinghua-Peking Center for Life Sciences, Beijing Frontier Research Center for Biological Structure, McGovern Institute for Brain Research, State Key Laboratory of Membrane Biology, School of Life Sciences and MOE Key Laboratory for Protein Science, Tsinghua University, Beijing, China

[5]These authors contributed equally to this work.

*Corresponding author.

Email: chengtian_zhao@ouc.edu.cn

ABSTRACT

How cells regulate the size of their organelles remains a fundamental question in cell biology. Cilia, with their simple structure and surface localization, provide an ideal model for investigating organelle size control. However, most studies on cilia length regulation are primarily performed on several single-celled organisms. In contrast, the mechanism of length regulation in cilia across diverse cell types within multicellular organisms remains a mystery. Similar to humans, zebrafish contain diverse types of cilia with variable lengths. Taking advantage of the transparency of zebrafish embryos, we conducted a comprehensive investigation into intraflagellar transport (IFT), an essential process for ciliogeneis. We observed IFT in multiple types of cilia with varying lengths. Remarkably, cilia exhibited variable IFT speeds in different cell types, with longer cilia exhibiting faster IFT speeds. The increased IFT speed in longer cilia was not due to changes in common factors that regulate IFT, such as motor selection, BBS proteins, or tubulin modification. Instead, longer cilia can organize larger IFT particles for faster transportation. Reducing the size of IFT particles can slow down IFT speed, resulting in shorter cilia. Our study presents an intriguing model of cilia length regulation via controlling IFT speed through the modulation of the size of the IFT complex. This discovery may provide further insights into our understanding of how organelle size is regulated in higher vertebrates.

INTRODUCTION

Understanding how cells regulate the size of their organelles is a fundamental question in cell biology. However, the three-dimensional complexity of most organelles poses challenges for accurate measurement, and thus, the underlying regulation mechanisms remain largely elusive. In contrast to the localization of most organelles within cells, cilia (also known as flagellar) are microtubule-based structures that extend from the cell surface, facilitating a more straightforward quantification of their size. Cilia are highly conserved organelles found across various organisms, ranging from protozoa to humans. Their formation relies on microtubules, and their size can be easily measured by their length, making cilia an ideal model for studying size regulation of sub-cellular organelles within the same organisms (Chan and Marshall, 2012).

Cilia play a crucial role in regulating various physiological and biochemical processes (Goetz and Anderson, 2010; Nachury and Mick, 2019; Singla and Reiter, 2006). Structural or functional abnormalities of this organelle can result a wide range of human genetic disorders, including retinal degeneration, polycystic kidneys, and mental retardation (Mill et al., 2023; Reiter and Leroux, 2017; Song et al., 2016). The assembly and maintenance of cilia rely on an elaborate process known as intraflagellar transport (IFT) (Kozminski et al., 1993). The IFT complex is located between the doublet microtubules of the cilia and the ciliary membrane, playing a vital role as a mediator of cargo transportation within cilia (Bhogaraju et al., 2013; Hesketh et al., 2022; Meleppattu et al., 2022). The IFT complex consists of two subcomplexes: the IFT-B complex, which transports the precursors required for cilia assembly from the base to the tip, powered by Kinesin-2; and the IFT-A complex, which transports axonemal turnover products back to the cell body by binding to dynein (Kardon and Vale, 2009; Ou et al., 2007; Scholey and J., 2008; Taschner et al., 2012). Electron microscopy studies have suggested that multiple IFT particles move together along the axoneme,

earning the name "IFT trains" (Jordan et al., 2018; Kozminski et al., 1995; Stepanek and Pigino, 2016). In *Caenorhabditis elegans*, both the slow-speed heterotrimeric kinesin II and the fast-speed homodimeric kinesin OSM-3 coordinate IFT, ensuring the assembly of sensory cilia (Snow et al., 2004). The IFT system also interacts with the BBSome complex, dysfunction of which is associated with the human ciliopathy Bardet-Biedl syndrome. The BBSome complex is moved by IFT and functions to maintain the physical connection between IFT-A and IFT-B subcomplexes in *C. elegans* (Ou et al., 2005). Moreover, the BBSome is involved in diverse functions, including protein trafficking into and out of the cilia. (Berbari et al., 2008; Jin et al., 2010; Lechtreck et al., 2009; Liu et al., 2021; Nachury et al., 2007; Ye et al., 2018).

The intraflagellar transport system plays a crucial role in ciliogenesis and is highly conserved across various organisms. Interestingly, the length of cilia exhibits significant diversity in different models. For example, *Chlamydomonas* has two flagella with lengths ranging from 10 to 14 μm, while sensory cilia in *C. elegans* vary from approximately 1.5 μm to 7.5 μm. In most mammalian cells, the primary cilium typically measures between 3 and 10 μm. Considering the conserved structure of cilia, it becomes intriguing to understand how their length is regulated in different cell types. Extensive research into flagellar length regulation has been conducted in *Chlamydomonas*. After one or two flagella are abscised, the shorter flagella can regenerate to their original length. During this regeneration process, the short flagella undergo a rapid growth phase, transitioning to a slower elongation phase as they approach their steady-state length (Rosenbaum et al., 1969). IFT plays a central role in mediating flagellar regeneration and IFT particles usually assemble into 'long' and 'short' trains within the flagella. At the onset of flagellar growth, long trains are prevalent, while the number of short trains gradually increases as the flagellum elongates (Engel et al., 2009; Vannuccini et al., 2016). Moreover, the rate at which IFT trains enter the flagella, known as the IFT injection rate, is negatively correlated with flagellar length during regeneration (Engel et al., 2009; Ludington et al., 2013). Researchers have proposed and tested several theoretical models to explain the regulatory mechanism of the IFT injection rate (Ishikawa et al., 2023; Marshall, 2023; Wemmer et al., 2020). Intriguingly, recent studies in the parasitic protist Giardia, which possesses eight flagella of varying lengths, revealed that the ciliary tip localization of microtubule-depolymerizing kinesin-13 is inversely correlated with flagellar length, similar to its role in flagellar length regulation (McInally et al., 2019; Piao et al., 2009; Wang et al., 2013). These findings add another layer of complexity to our understanding of ciliary length regulation and underscore the importance of investigating diverse model organisms to gain comprehensive insights into this fundamental biological process.

Notably, most studies on ciliary length control have focused on single-celled organisms. However, in vertebrates, the presence of highly diverse cell types results in cilia of varying lengths. Understanding how cilia length is regulated in different cell types and why such diversity exists is essential for comprehending the pathogenic mechanisms underlying various organ defects seen in ciliopathies. Unfortunately, direct observation of intraflagellar transport (IFT) in living vertebrates has posed challenges, limiting our knowledge in this area.

In this study, we capitalized on the benefits of embryonic transparency in zebrafish to explore dynamic IFT in various types of cilia. To the best of our knowledge, this is the first report of IFT

investigation in multiple organs within a living organism. Our findings revealed a positive correlation between the speed of IFT transport and cilia length. Furthermore, ultra-high-resolution microscopy showed a close association between cilia length in different organs and the size of IFT fluorescent particles, indicating the presence of larger IFT trains in longer cilia. This observation suggests that cargo and motor proteins are more effectively coordinated in transporting materials, resulting in increased IFT velocity—a novel regulatory mechanism governing IFT speed in vertebrate cilia.

Results and Discussion

Zebrafish provide an ideal model to compare ciliogenesis in different organs

Similar to humans, cilia are widely present in various organs in zebrafish. Utilizing an Arl13b-GFP transgene under the control of the beta-actin promoter, we can observe cilia in live embryos within organs such as Kupffer's vesicle, ear, lateral line, spinal cord, and skin. Cilia in the pronephric duct, olfactory pit, photoreceptor cells, and sperms can be visualized through antibody staining with acetylated-tubulin. Notably, the number and length of cilia exhibit significant variation across different tissues (Fig 1). While most cells contain a single cilium, certain specialized cell types, including olfactory epithelia and pronephric duct, form multiple cilia. In adult zebrafish, multiciliated cells can also be found in the brain ventricles (ependymal cells) and ovary(Ogino et al., 2016). Consequently, zebrafish provides an ideal model for investigating ciliogenesis in diverse cell types (Song et al., 2016).

Rescue of *ovl* (*ift88*) mutants with *Tg(hsp70l:ift88-GFP)* transgene

To visualize IFT in zebrafish, we first generated a stable transgenic line, *Tg(hsp70l:ift88-GFP)*, which expresses a fusion protein of Ift88 and GFP under the control of the heat shock promoter (Fig. 2A). Ift88 plays a crucial role as a component of the IFT complex in maintaining ciliogenesis. Zebrafish *ovl* mutants exhibited body curvature defects and typically do not survive beyond 7 days post-fertilization (dpf) (Tsujikawa and Malicki, 2004). By performing a daily heat shock starting from 48 hours post-fertilization (hpf), we observed that the body curvature defects were completely rescued at 5dpf (Fig 2B, C). Furthermore, we assessed ciliogenesis defects in these mutants. At 5 dpf, cilia were absent in most tissues of the *ovl* mutants (Fig. 2D). In contrast, this transgene effectively rescued ciliogenesis defects in all examined tissues (Fig. 2D and S1A). Interestingly, the GFP fluorescence of the transgene was prominently enriched in the cilia (Fig 1D). Additionally, we conducted continuous heat shock experiments, which showed that *ovl* mutants carrying this transgene were able to survive to adulthood (Fig. S1B). Taken together, these findings demonstrate that Ift88-GFP can substitute for endogenous Ift88 in promoting ciliogenesis.

Visualization of IFT in different cilia

The enrichment of Ift88-GFP within cilia implies that the *Tg(hsp70l: ift88-GFP)* transgene could serve as a valuable tool for real-time observation of IFT movement (Fig 2D). Despite cilia typically being situated in the deep regions of the body, we managed to detect the movement of GFP fluorescence particles using a high-sensitive spinning-disc microscope. First, we focused on ear cristae hair cell cilia which are longer and easy to detect. We succeeded in the direct visualization of the movement of fluorescent particles in these cilia (Movie S1). Kymograph analysis revealed bidirectional movement of the Ift88-GFP particles along the cilia axoneme (Fig 3A), akin to IFT movements observed in other species (Kozminski et al., 1993; Orozco et al., 1999). Moreover, we also captured the dynamic movement of these Ift88-GFP particles in various cilia, including those of neuromasts, pronephric duct, spinal cord, and skin epidermal cells (Fig 3B-E, Movies S2-5). These movies provide a great opportunity to compare IFT across different cilia.

Correlation between IFT speed and ciliary length

To characterize the dynamics of IFT, we quantified their movement speed using kymographs

generated from recorded movies (Fig. 3F, G). Within each type of cilia, the retrograde IFT showed higher speed compared to anterograde transport, consistent with previous findings in *C. reinhardtii* and *C. elegans*, where dynein motors were found to move faster than Kinesin motors. Surprisingly, we observed significant variability in IFT velocities among different cilia. In ear crista cilia, the average speed of anterograde IFT was 0.68 μm/s, while in the cilia of neuromast hair cells, it decreased to 0.54 μm/s. In skin epidermal cilia and spinal canal cilia, the transport rates were further reduced to 0.42 μm/s and 0.33 μm/s, respectively. The pronephric duct cilia showed intermediate average anterograde IFT rates at 0.46 μm/s. Similarly, retrograde transport also displayed considerable variability, with ear crista and neuromast cilia exhibiting the highest speeds (1.55 μm/s and 1.47 μm/s, respectively). In contrast, cilia in the spinal canal showed the slowest IFT, with an average speed of 0.35 μm/s, which was less than one fourth of the speed observed in ear crista cilia (Fig 3G).

Both anterograde and retrograde IFT displayed remarkably high transport speeds in ear crista and neuromast cilia. Intriguingly, we observed that these cilia were particularly longer compared to others. To investigate this correlation further, we compared ciliary length in different tissues and discovered a strong correlation between cilia length and IFT speeds (Fig 3H, I). Specifically, longer cilia demonstrated faster IFT rates in both the anterograde and retrograde directions. Interestingly, longer cilia also have a higher frequency of fluorescent particles entering cilia (Fig 3J). These findings establish a compelling link between ciliary length and IFT speeds, suggesting a potential functional significance. To validate this relationship further, we created an additional transgenic line, *Tg(βactin2: tdTomato-ift43),* which allowed us to label Ift43, a constituent of the IFT-A complex. Through the analysis of Ift43 transport in this transgenic line, we reaffirmed that the tdTomato-Ift43 fluorescence particles also exhibited the highest transport speeds in ear crista cilia (Fig S2).

IFT in the absence of Kif17 or Bbs proteins

To understand the potential mechanisms underlying the variation in IFT speeds among different cilia, we initially focused on differences in motor proteins. In *C. elegans*, the homodimeric kinesin-2, OSM-3, drives the IFT complex at a relatively higher speed compared to the heterotrimeric Kinesin-2 (Ou et al., 2005). We examined IFT in *kif17* mutants, which carry a mutation of the fast homodimeric kinesin (Zhao et al., 2012). Surprisingly, in the absence of Kif17, the IFT speeds remained similar to those of control larvae (Fig 4A, B, S3, Movie S6, Table S1). Similarly, the IFT maintained regular speed in the absence of Kif3b in the ear crista(Fig 4A, B, Movie S7, Table S1), possibly due to the redundant function of Kif3c in the heterotrimeric Kinesin-2 (Zhao et al., 2012). Additionally, we assessed IFT in the *bbs4* mutants, which has been proposed to affect the connection between the two IFT subunits in *C. elegans*. Once again, the Bbs4 mutation had little effect on IFT motility (Fig 4A, B, S3, Movie S8, Table S1). Thus, these data suggest that the variability in IFT speeds among different cilia cannot be attributed to the use of different motor proteins or the involvement of the BBSome complex.

Tubulin modifications, ATP concentration and IFT

IFT was driven by kinesin or dynein motor proteins along the ciliary axoneme. The post-translational modifications of axonemal tubulins can affect the interaction between microtubules

and motor proteins, thereby regulating their dynamics (Hong et al., 2018; Janke and Bulinski, 2011; O'Hagan et al., 2017; Sirajuddin et al., 2014). Next, we asked whether tubulin modifications can affect IFT in zebrafish. Ttll3 is a tubulin glycylase that are involved in the glycylation modification of ciliary tubulin (Wloga et al., 2009). We generated zebrafish *ttll3* mutants and identified a mutant allele with an 8bp insertion, which causes frameshift, resulting in a significantly truncated Ttll3 protein without TTL domain (Fig. 4C,D). Immunostaining with anti-monoglycylated or polyglycylated tubulin antibody revealed that the glycylation modification was completely eliminated in all the cilia investigated (Fig. 4E and S4). Surprisingly, there are no obviously defects in the number and length of cilia in the mutants. The velocity of IFT within different cilia was also seems unchanged (Fig. 4F, Movie S9, Table S1). Moreover, the mutants were able to survive to adulthood and there is no difference in the fertility or sperm motility between mutants and control siblings, which is slightly different to those observed in mouse mutants (Gadadhar et al., 2021).

Next, we investigated whether polyglutamylation of axonemal tubulins can regulate IFT movement in zebrafish. First, we knocked down the expression of *ttll6*, which has been shown early to reduce tubulin glutamylation and resulted in body curvature in zebrafish (Fig. S5A, B) (Pathak et al., 2011). The efficiency of *ttll6* morpholinos was confirmed via RT-PCR (reverse transcription-PCR), which showed the splicing error of intron 12 when introduced the morpholinos (Fig. S5C, D). Interestingly, we observed only minor differences in IFT velocity between *ttll6* morphants and control groups (Fig 4G, Table S1). Similarly, the IFT speeds also exhibited only slightly changes in *ccp5* morphants, which decreased the deglutamylase activities of Ccp5 and resulted in a hyper-glutamylated tubulin (Fig. 4G and S5E-H, Table S1) (Pathak et al., 2014). Together, these results suggest that tubulin codes may play relatively minor roles on IFT in zebrafish. Considering the big difference in the IFT speed among different cilia, we think it is very unlikely such difference is caused by different levels of tubulin modification.

The movement of kinesin and dynein motors relies on the energy derived from ATP hydrolysis. In vitro studies using molecular force clamp techniques have shown that increasing ATP concentration significantly enhances the speed of kinesin during cargo loading (Visscher et al., 1999). We further examined whether the difference of IFT speeds was caused by variation of ATP concentration inside cilia. We generated an ATP reporter line, *Tg (βactin2: arl13b-mRuby-iATPSnFR$^{1.0}$)*, which contains a ciliary localized ATP sensor, mRuby-iATPSnFR$^{1.0}$ driven by b-actin2 promotor (Fig. S6A-B) (Lobas et al., 2019). This ATP sensor utilizes relative fluorescence intensity to indicate the concentration of ATP. By measuring the ratio of mRuby red fluorescence to green fluorescence in the longer crista and shorter epidermal cilia, we compared relative ATP levels between these two types of cilia. Again, we found no difference in the ATP concentration between crista and epidermal cilia, suggesting that variation of ATP concentration was unlikely to be the cause of different IFT speed (Fig. S6C).

Larger IFT particles in longer cilia

Finally, we aim to investigate the size of IFT particles within different type of cilia. In the flagellar of *Chlamydomonas*, IFT particles are usually transported as IFT trains, consisting of multiple IFT-A and IFT-B repeating subcomplexes and the kinesin-2 and IFT dynein motors. However, with current technique, it is unfeasible to distinguish the size of IFT trains on different type of cilia through ultra-structure electron microscopy in zebrafish. Instead, we sought to compare the size of the fluorescence particles using STED ultra-high-resolution microscopy. With this method, we were able to identify single IFT fluorescence particles with relatively high resolution. Compared with regular spinning disk data, the number of IFT fluorescence particles was significantly increased in the cilia (Fig 5A, B). When comparing the size of these fluorescence particles, we found that the particle sizes were significantly larger in the longer crista cilia than those of the shorter spinal cord cilia (Fig. 5C).

To further test whether the higher IFT velocity was associated with large IFT particles in the crista cilia, we performed morpholino based knockdown analysis. Injection of *ift88* morpholino caused body curvature due to ciliogenesis defects (Fig 5D). When injecting lower dose of *ift88* morpholino, we found zebrafish embryos can still maintain grossly normal body axis, while cilia in ear crista became significantly shorter (Fig 5D, E, I). Due to partial loss of Ift88 proteins, the number of IFT complex decreased significantly as suggested by the reduced number of IFT fluorescence particles in the morphant cilia (Fig 5F, G). Noticeably, the size of the fluorescent particles also decreased significantly, implying a potentially reduced length of the IFT trains (Fig. 5F, H). Strikingly, we found the IFT speed also decreased significantly in the shorter cilia (1.55 μm/s in control vs 1.18 μm/s in morphants) (Fig 5I, J, Movie S10). Taken together, these data strongly suggested that the size of IFT fluorescence particles is closely related to IFT speed and longer cilia are prone to contain larger IFT particles than shorter cilia.

A hypothetical model of cilia length regulation in zebrafish

With its diverse array of cilia types, zebrafish provide an exceptional model for investigating the intricate mechanisms underlying ciliary length regulation. By creating a transgenic line that expresses ciliary-targeted IFT proteins, we have demonstrated a positive correlation between IFT transport speed and the length of cilia. To the best of our knowledge, this study represents the first instance of comparing IFT transport in cilia from different types of organs within the same organism. Interestingly, certain conventional factors known to govern IFT transport regulation in *C. elegans* or *Chlamydomonas* appear to exert limited influence in zebrafish. Firstly, IFT transport speed showed no discernible connection to ciliary motility, as evidenced by the comparable IFT speeds observed in both motile spinal cord cilia and primary cilia of the skin's epidermal cells (Fig 3). Furthermore, the accelerated IFT transport cannot be attributed to distinct motor utilization, BBS proteins, or tubulin modifications, all of which have been suggested to regulate IFT transport in worms. Surprisingly, tubulin glycylation is not only non-essential for IFT transport but also dispensable for zebrafish development, as zebrafish *ttll3* mutants are viable and fertile. Collectively, these results suggest that the regulation of IFT velocity in zebrafish cilia differs from that observed in *C. elegans*, thereby highlighting the intricate complexity of IFT regulation across various organisms.

Remarkably, our studies revealed that the IFT fluorescence particles were significantly larger in longer crista cilia than those of shorter cilia. The IFT complex typically travels as trains, with multiple repeating IFT units being transported simultaneously. The increased size of the fluorescence particles implies that longer cilia might form larger IFT trains for more effective cargo transportation. Decreasing the quantity of IFT88 proteins could diminish the likelihood of IFT complex assembly, consequently leading to a reduction in the size of IFT trains. Importantly, the size of IFT particles was significantly reduced in *ift88* morphants, concurrent with the decreased transport speed of IFT. Thus, our data support a length control model for cilia that operates through the modulation of IFT train size (Fig 5K). Within longer cilia, the IFT complex appears predisposed to form lengthier repeating units, thereby creating an optimal platform for efficient transport. This environment enhances the coordination between cargos and motor proteins, resulting in an improved transportation speed. This orchestration potentially involves the synchronization of motor proteins, ensuring their precise functionality and directional alignment during transport—a concept supported by various models (Stukalin et al., 2005; Urnavicius et al., 2018). Furthermore, insights from the cryo-EM structure of intraflagellar transport trains have suggested that each dynein motor protein might propel multiple IFT complexes. For instance, the ratio of dynein: IFT-B: IFT-A in the flagella of *Chlamydomonas* is approximately 2:8:4 (Jordan et al., 2018). It remains plausible that longer cilia in vertebrates could recruit a higher ratio of motor proteins to execute IFT, thus intensifying the driving force for cargo transport. The mechanisms behind achieving these conditions may require further investigation.

Materials and methods

Ethics statement

All zebrafish study was conducted according standard animal guidelines and approved by the Animal Care Committee of Ocean University of China (Animal protocol number: OUC2012316).

Zebrafish Strains

All zebrafish strains were maintained following standard protocols. The following mutant strains were used: *ovl* (Tsujikawa and Malicki, 2004), *kif3b* and *kif17* (Zhao et al., 2012). Three transgenic lines, *Tg(hsp70l:ift88-GFP), Tg(βactin2:tdTomato-ift43)* and *Tg (βactin2: arl13b-mRuby-iATPSnFR$^{1.0}$),* were generated in this study. The constructs for making these transgene were created using Tol2 kit Gateway-based cloning (Kwan et al., 2007). The *ttll3* mutants were generated via CRISPR/Cas9 technology with the following target sequence: 5'-GGGTGGAGCGGCGATTGCCA-3'. The *bbs4* mutants were generated by TALEN system with the following binding sequences: 5'-TAAACTTGGCATTACAGC-3' and 5'-TCCCAGCATCATGTAGGTC -3'. All strains involved are stable lines.

IFT imaging and analysis

For crista cilia imaging, zebrafish larvae were anesthetized with 0.01% Tricaine in E3 water and then embedded in 1.25% low melting point agarose on a confocal dish. When imaging cilia in neuromast, epidermal cells, spinal cord, or pronephric duct epithelial cells, the embryos were anesthetized and placed on a confocal dish. Excess water was carefully removed, and a circular cover glass was then placed over the sample for imaging. IFT movements in crista cilia and

neuromast were recorded using an Olympus IX83 microscope equipped with a 60X, 1.3 NA objective lens, an EMCCD camera (iXon+ DU-897D-C00-#BV-500; Andor Technology), and a spinning disk confocal scan head (CSU-X1 Spinning Disk Unit; Yokogawa Electric Corporation). Time-lapse images were continuously collected with 100 or 200 repeats using μManager (https://www.micro-manager.org) at an exposure time of 200 ms. Kymographs were generated using Image J software. IFT Movement in cilia of epidermal cells, spinal cord, and pronephric duct epithelial cells were recorded using an Olympus IX83 microscope equipped with a 100X, 1.49 NA objective lens, and the same EMCCD camera and spinning disk confocal modules as mentioned above.

Whole-mount Immunofluorescence

Zebrafish larvae were fixed overnight at 4°C in 4% PFA. After removing the fixative, they were washed three times with PBS containing 0.5% Tween 20 (PBST) and then incubated in acetone for 10 minutes for permeabilization. Subsequently, the embryos were treated with a blocking reagent (PBD with 10% goat serum) for 1 hour and sequentially labeled with primary and secondary antibodies (at a 1:500 dilution) overnight at 4 °C. The following antibodies were used: anti-acetylated α-tubulin (Sigma T6793), anti-monoglycylated tubulin antibody, clone TAP 952 (Sigma MABS277), anti-polyglycylated tubulin antibody, clone AXO49 (Sigma MABS276), anti-GFP (Invitrogen A-11120), and anti-HA (Invitrogen).

Morpholino knockdown

The following morpholinos were used: *ttll6* (5' - GCAACTGAATGACTTACTGAGTTTG - 3'), *ccp5* (5' -TCCTCTTAATGTGCAGATACCCGTT-3') and a standard control morpholino (5' - CCTCTTACCTCAGTTACAATTTATA-3'). All morpholinos were purchased from Gene Tools (Philomath, OR). To detect splicing defects caused by morpholinos, we extracted total RNA from 24hpf embryos and performed RT-PCR using the following primer sequences: *ttll6* Forward: 5'-AAAGTATTTCCAACACAGCAGCTC-3', Reverse: 5'-GTGGTCGTGTCTGCAGTGTGGAGG-3'; *ccp5* Forward: 5'-TCCTGTCGTTTGTTCATCGTCTGC-3', Reverse: 5'-CTTAAAGACGAACATGCGGCGAAG-3'

Super-resolution microscopy

High resolution images were acquired using Abberior STEDYCON (Abberior Instruments GmbH, Göttingen, Germany) fluorescence microscope built on a motorized inverted microscope IX83 (Olympus UPlanXAPO 100x, NA1.45, Tokyo, Japan). The microscope is equipped with pulsed STED lasers at 775 nm, and with 561 nm and 640 nm excitation pulsed lasers. Zebrafish larvae were collected and fixed in 4% PFA overnight at 4°C. For STED imaging, the following secondary antibody were used: goat anti-mouse Abberior STAR RED and goat anti-rabbit Abberior STAR ORANGE. The embryos were incubated in secondary antibody(1:100) in blocking buffer at room temperature for 2 h. After wash three times (5 min each) with PBST, larvae were cryoprotected in 30% sucrose overnight. Sagittal sections were collected continuously at 40 μm thickness on Leica CM1850 cryostat. Place the slices at 37 degrees for 1 hour to dry. Rehydrate in PBST for 5 min and cover with Abberior Mount Liquid Antifade. After sealing, the slices were placed at 4 °C overnight before imaging.

Statistical analysis

Statistical analysis was performed using GraphPad Prism 8 software. ImageJ software was used to measure length of cilia, fluorescence intensity and particle size. Statistical significance was evaluated by means of the two-tailed Student t-test for unpaired data.

Acknowledgments

We thank Dr. Guangshuo Ou and members of the Zhao lab for their kind help during the preparation of this manuscript. We are also grateful for the excellent support from the core facilities of IEMB at OUC. This work was supported by the National Natural Science Foundation of China (Nos. 32125015, 31991194 to C.Z. and No. 32100661) to H.X.) to C.Z..

Figures and legends

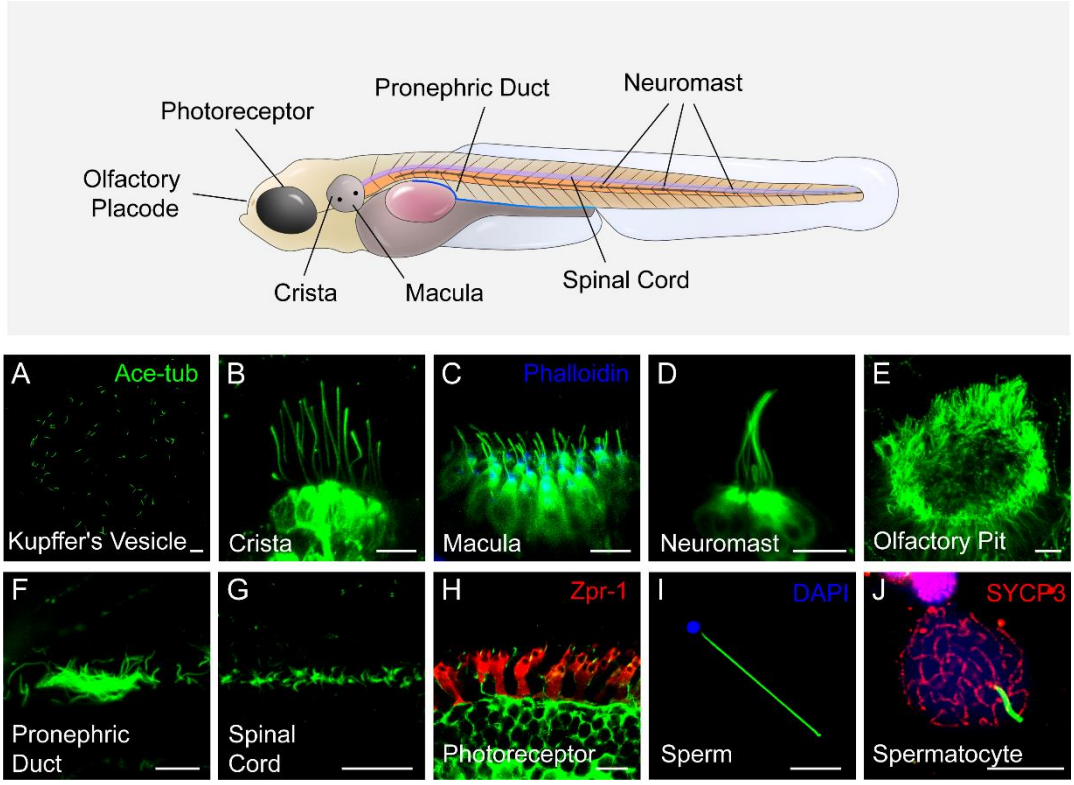

Fig 1 Diverse type of cilia are present in zebrafish

(A) Cilia in the kupffer's vesicle (KV) of a 10-somite stage zebrafish larvae. (B-H) Confocal images showing cilia in different type of cells as indicated. The position of these cells were indicated in the top diagram. (I-J) Confocal images showing cilia in the sperm (flagellum) or spermatocyte. All the cilia were visualized with anti-acetyleated tubulin antibody. Scale bar=10 μm.

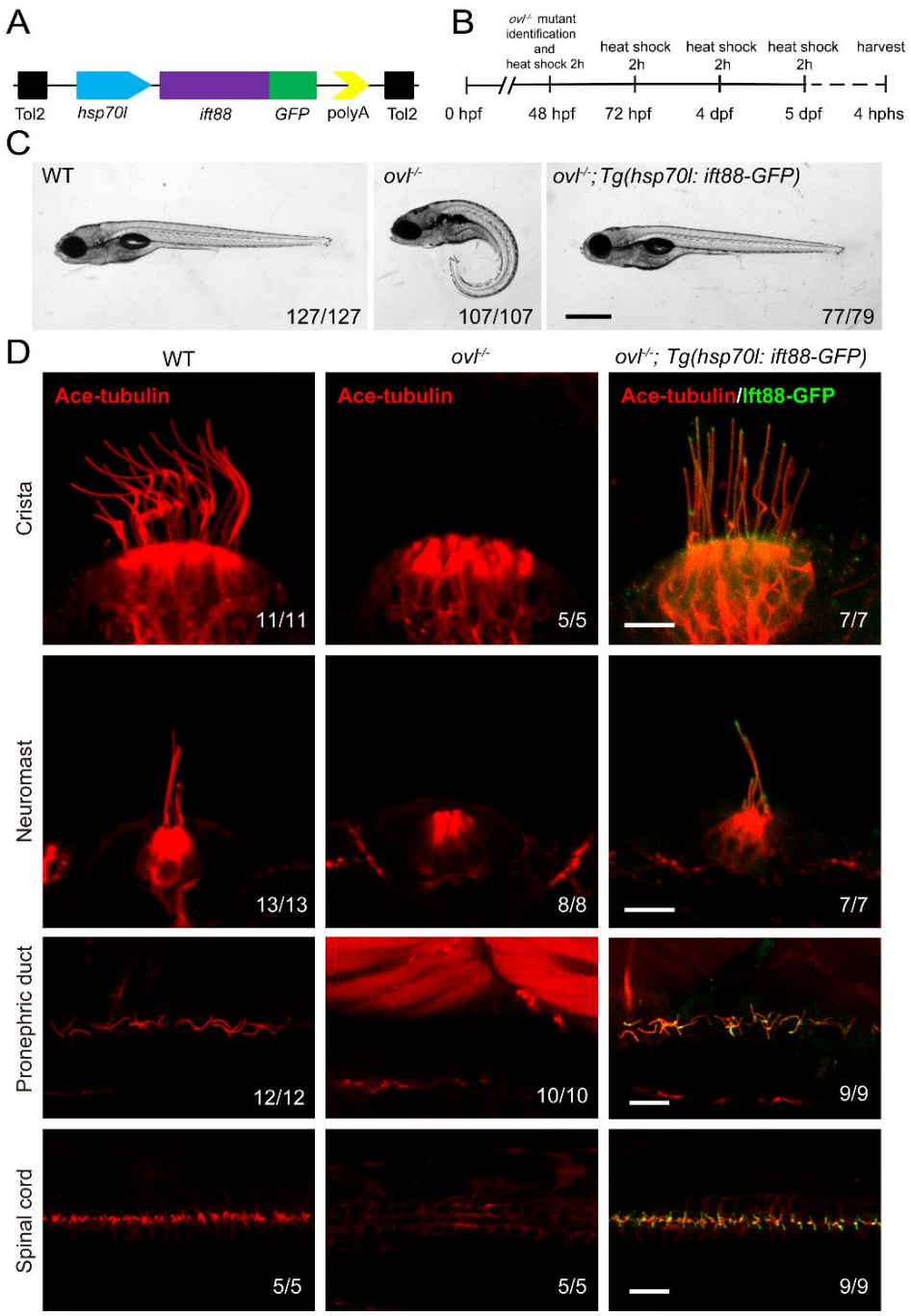

Fig 2 Rescue of *ovl* mutants with Tg(*hsp70l:ift88-GFP*) transgene.

(A) Schematic diagram of *hsp70l:ift88-GFP* construct. (B) Procedure of heat shock experiments for *ovl* mutants rescue assay. (C) External pheontype of 3dpf wild type, *ovl* mutant or *ovl* mutant larvae carrying Tg(*hsp70l:ift88-GFP*) transgene. The numbers of larvae investigated were shown on the bottom right. (D) Confocal images showing cilia in different type of organs as indicated.

Red channel indicates cilia visualized by anti-acetylated α-tubulin antibody and fluorescence of *Tg(hsp70l:ift88-GFP)* is showed in green. Scale bars: 200 μm in panel C and 10 μm in panel D.

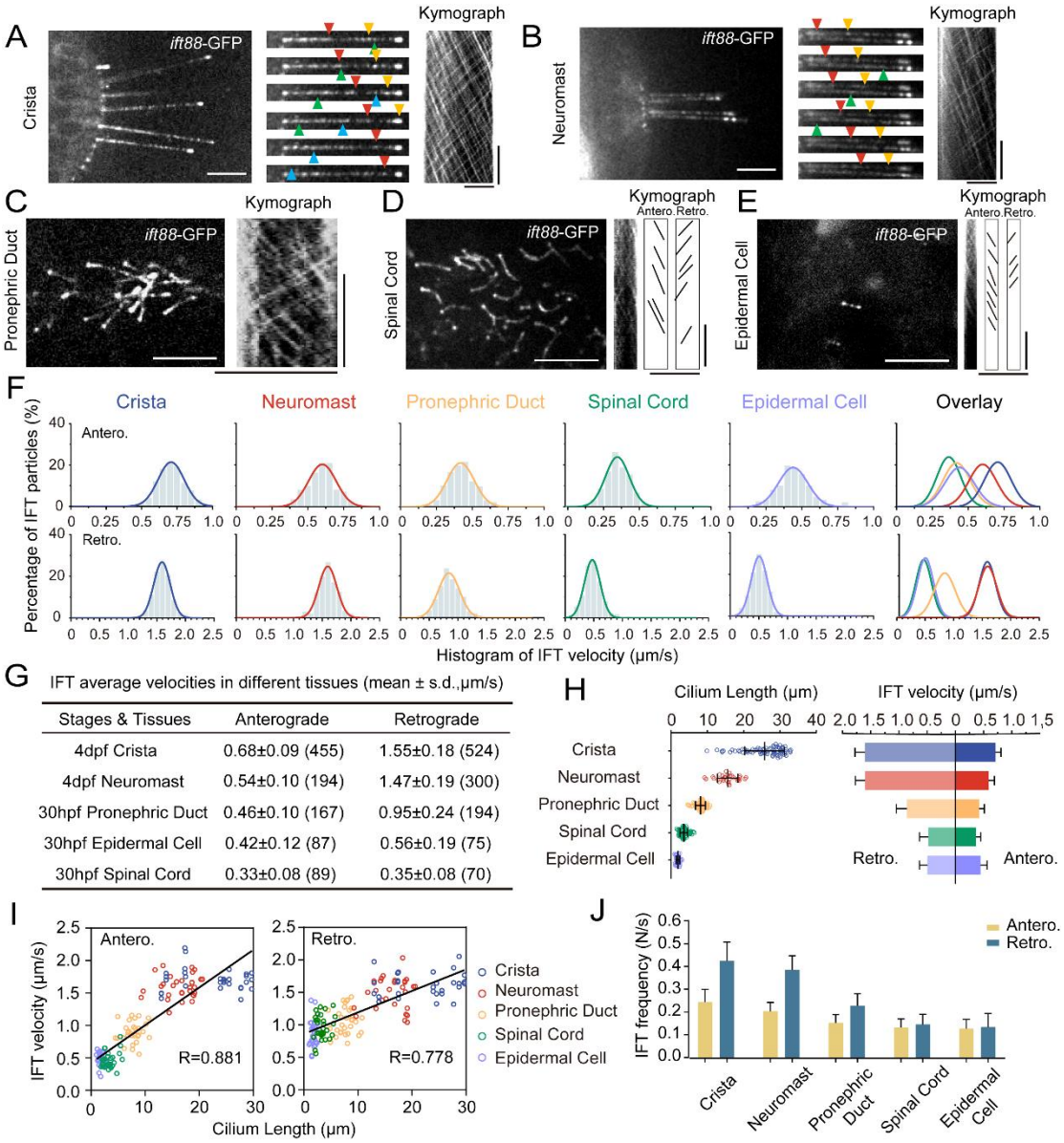

Stages & Tissues	Anterograde	Retrograde
4dpf Crista	0.68±0.09 (455)	1.55±0.18 (524)
4dpf Neuromast	0.54±0.10 (194)	1.47±0.19 (300)
30hpf Pronephric Duct	0.46±0.10 (167)	0.95±0.24 (194)
30hpf Epidermal Cell	0.42±0.12 (87)	0.56±0.19 (75)
30hpf Spinal Cord	0.33±0.08 (89)	0.35±0.08 (70)

Fig 3 Intraflagellar transport in different type of cilia.

(A-E) Left, Snapshot of Intraflagellar transport videos in different cell types as indicated. Middle (A, B), Snapshot of same cilia at different time points. Arrowheads with the same color indicate the same IFT particle. Right, kymographs illustrating the movement of IFT particles along the axoneme. Horizontal scale bar: 10 μm and vertical scale bars: 10 s. Representative particle traces are marked with white lines in panels D and E. (F) Histograms displaying the velocity of anterograde and retrograde IFT in different type of cilia as indicated. “Antero.” and “Retro.” represent anterograde and retrograde transport, respectively. (G) Summary of IFT velocities in different tissues of zebrafish. Numbers of IFT particles are shown in the brackets. (H) Left, Statistics analysis of cilia length in different tissues of zebrafish. Right, anterograde and retrograde IFT average velocity in different tissues of zebrafish. (I)Anterograde and retrograde IFT velocities plotted versus cilia length. Linear fit (black line) and coefficient of determination are indicated. (J) Frequency of anterograde and retrograde IFT entering or exiting cilia.

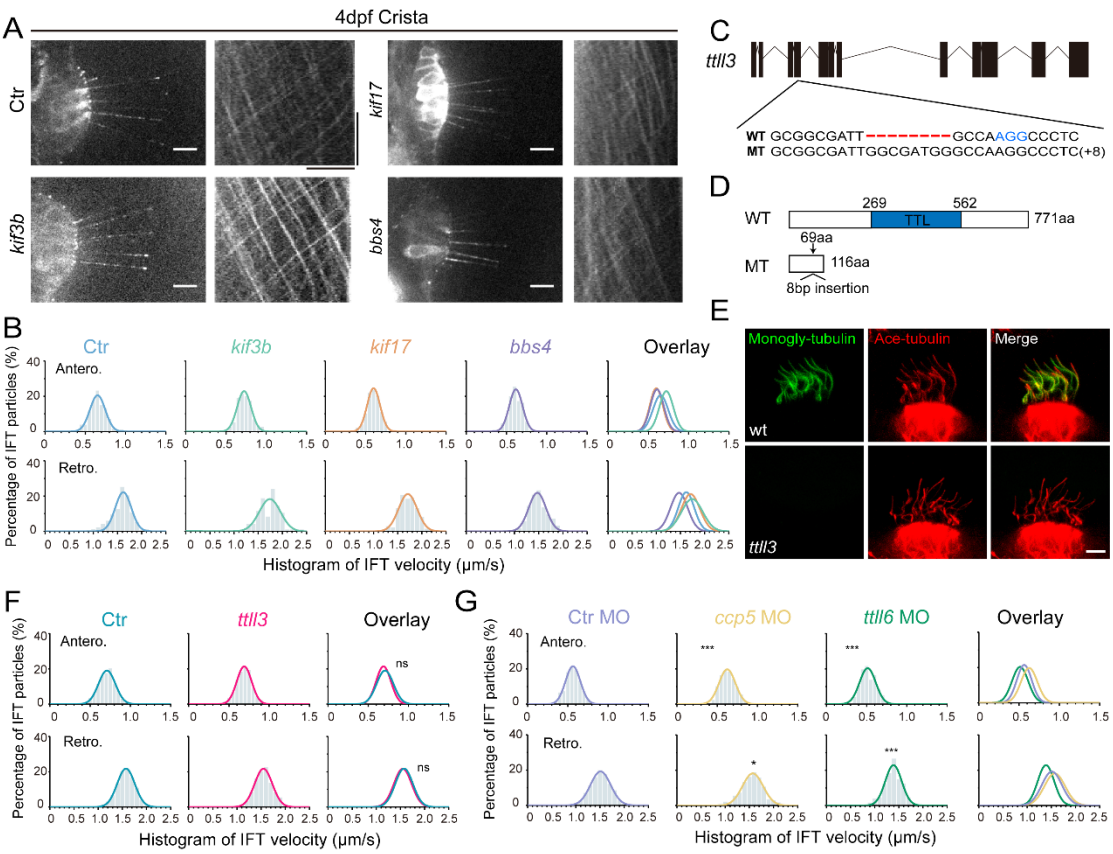

Fig 4. Alterations in motor proteins, BBS proteins, or tubulin modifications have minimal effects on IFT.

(A) Left: Snapshot of IFT videos in crista cilia of 4dpf wild type or mutant larvae as indicated. Right: Kymographs showing IFT particle movement along axoneme visualized with Ift88:GFP. Horizontal scale bar: 10μm and vertical scale bar:10s. (B) Histograms showing anterograde and retrograde IFT velocity in crista cilia of control or mutant larvae. (C) Genomic structure and sequences of wild type and *ttll3* mutant allele. PAM sequence of sgRNA target are indicated in blue. (D) Protein domain of Ttll3 in wildtype and *ttll3* mutants. (E) Confocal images showing crista cilia in wild-type or maternal-zygotic (MZ) *ttll3* mutants visualized with anti-monoglycylated tubulin antibody (green) and anti-acetylated α-tubulin antibody (red). (F) Histograms depicting IFT velocity in crista cilia of control and *ttll3* mutants. Top, anterograde IFT. Bottom, retrograde IFT. (G) Histograms illustrating IFT velocity in crista cilia of *ccp5* or *ttll6* morphants. Scale bars: 10 μm in panel A and 5 μm in panel E. *$p < 0.5$; *** $p < 0.001$.

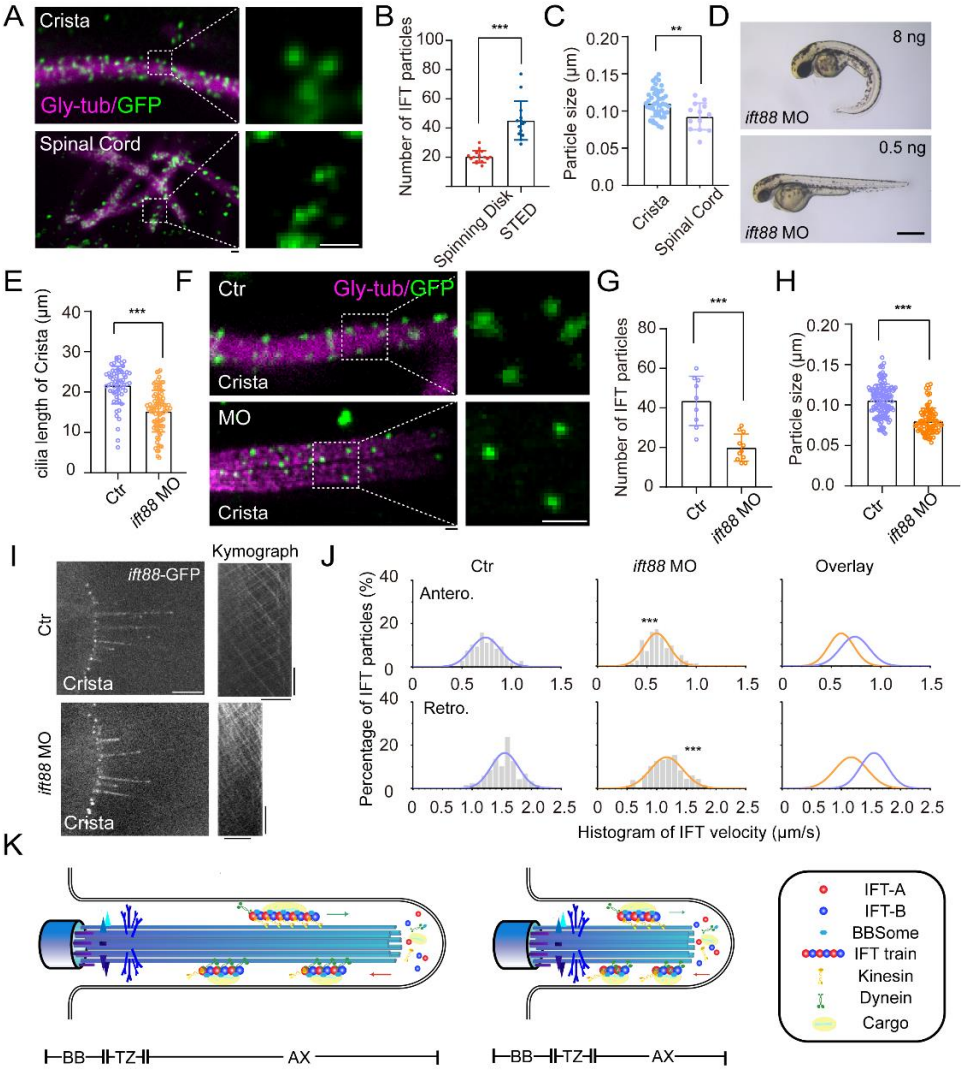

Fig 5 Increased size of IFT fluorescent particles in crista cilia.

(A) Representative STED images of crista (top) and spinal cord (bottom) in 4dpf *Tg(hsp70l: ift88-GFP)* larva. Cilia was stained with anti-monoglycylated tubulin (magenta), and IFT88-GFP particles were counterstained with anti-GFP antibody (green). Enlarged views of the boxed region are displayed on the right. (B) Dot plots showing the number of IFT particles per arbitrary unit (a.u.) in crista cilia recorded by spinning disk and STED. (C) Statistical analysis showing IFT particles size in the cilia of ear crista and spinal cord. (D) External phenotypes of 2 dpf zebrafish larvae injected with higher and lower dose of *ift88* morpholinos. (E) Statistical analysis of cilia length in control or *ift88* morphants. (F) STED images showing IFT particles in crista cilia of 3dpf control or *ift88* morphants. Enlarged views of the boxed region are displayed on the right. (G) Dot plots showing the number of IFT particles in control and *ift88* morphants. (H) Statistical analysis showing IFT particles size of crista cilia in control or *ift88* morphants. (I) Left, Snapshot of IFT videos in crista cilia of 3dpf control (top) or *ift88* morphant (bottom) carrying *Tg(hsp70l: ift88-GFP)*. Right, Kymographs showing movement of IFT particles along axoneme. Horizontal scale bar: 10μm and vertical scale bar:10s. (J) Histograms showing IFT velocity in 3dpf control or *ift88* morphants. (K) Model illustrating IFT with different train sizes in long and short cilia. Scale bars: 0.2 μm in panel A and F, and 500 μm in panel I. ** $p < 0.01$; *** $p < 0.001$.

Supplementary figures

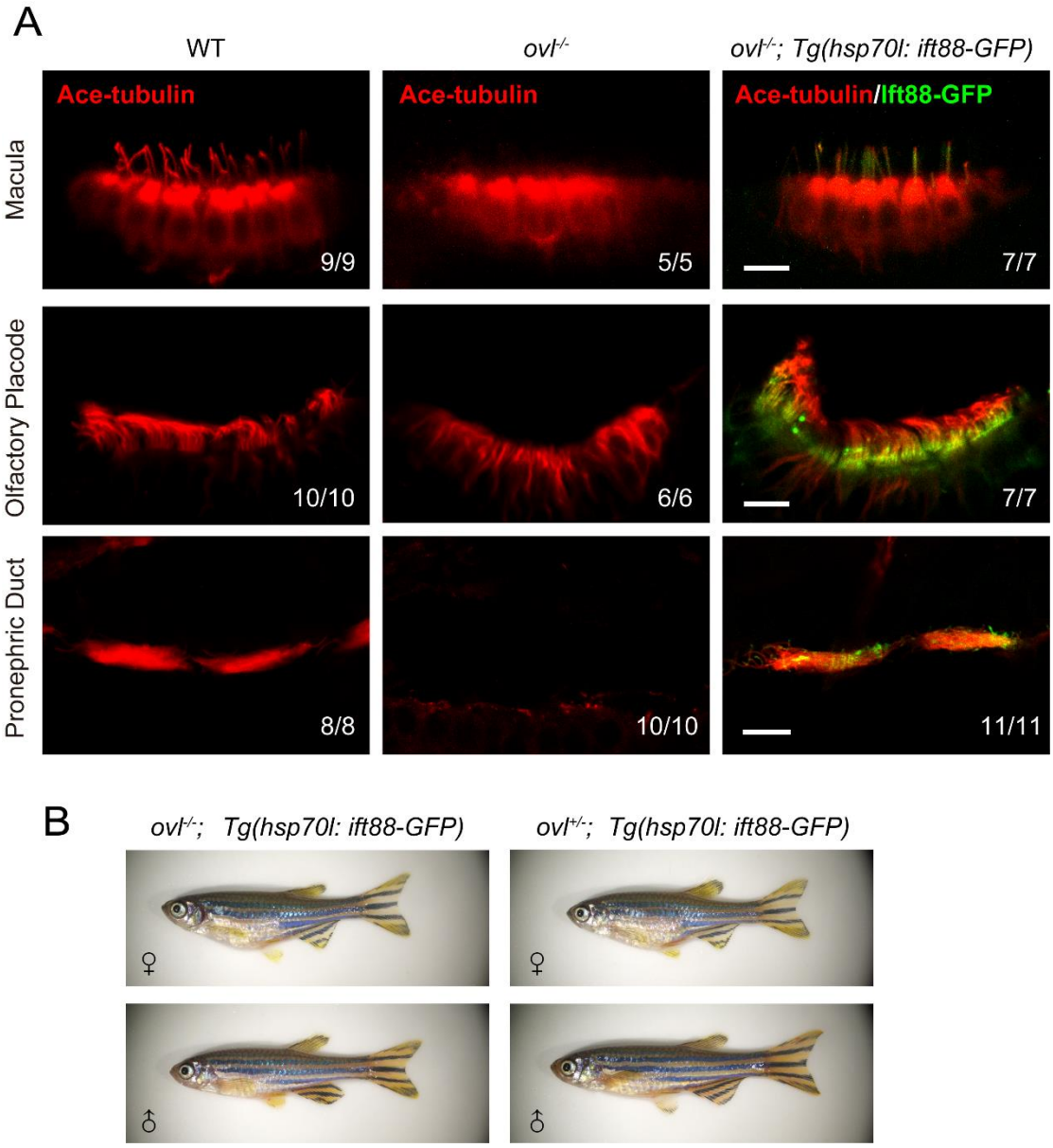

Figure S1 Rescue of ciliogenesis defects in *ovl* (*ift88*) mutants via *Tg(hsp70l:ift88-GFP)*

(A) Rescue of ciliogenesis defects in ear macula, olfactory placode and pronephric duct. MC, multicilia. Red channel shows cilia visualized by anti-acetylated α-tubulin antibody. Fluorescence of *Tg(hsp70l:ift88-GFP)* is showed in green. Scale bar=10μm. (B) External phenotypes of adult *ovl* homozygotes rescued with *Tg(hsp70l:ift88-GFP)* transgene.

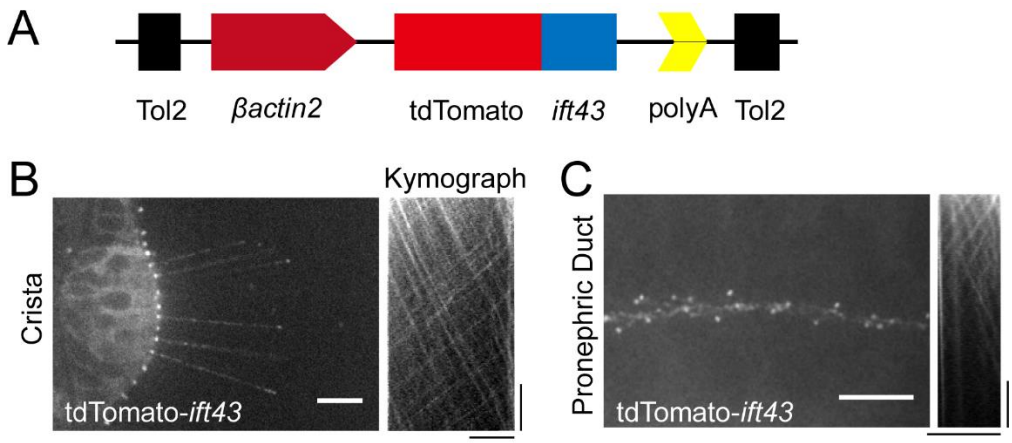

D

IFT Velocities (mean ± s.d.,μm/s)

Stages & Tissues	Anterograde	Retrograde
4dpf Crista	0.68±0.08 (160)	1.53±0.18 (126)
30hpf Pronephric Duct	0.39±0.09 (170)	0.78±0.16 (140)

Figure S2 Generation of Tg (*βactin2*:*tdTomato-ift43*) transgene for IFT imaging

(A) Schematic diagram showing *βactin2:tdTomato-ift43* transgenic construct. (B-C) Left, Snapshot of Intraflagellar transport videos in cilia of ear crista and pronephric duct epithelial cells. Right, kymographs illustrating the movement of IFT particles along the axoneme. Horizontal scale bar=10 μm. Vertical scale bar=10 s. (D) Summary of the anterograde and retrograde velocities of IFT measured in embryos expressing *Tg(βactin2:tdTomato-ift43)*. Numbers of IFT particles are shown in the brackets.

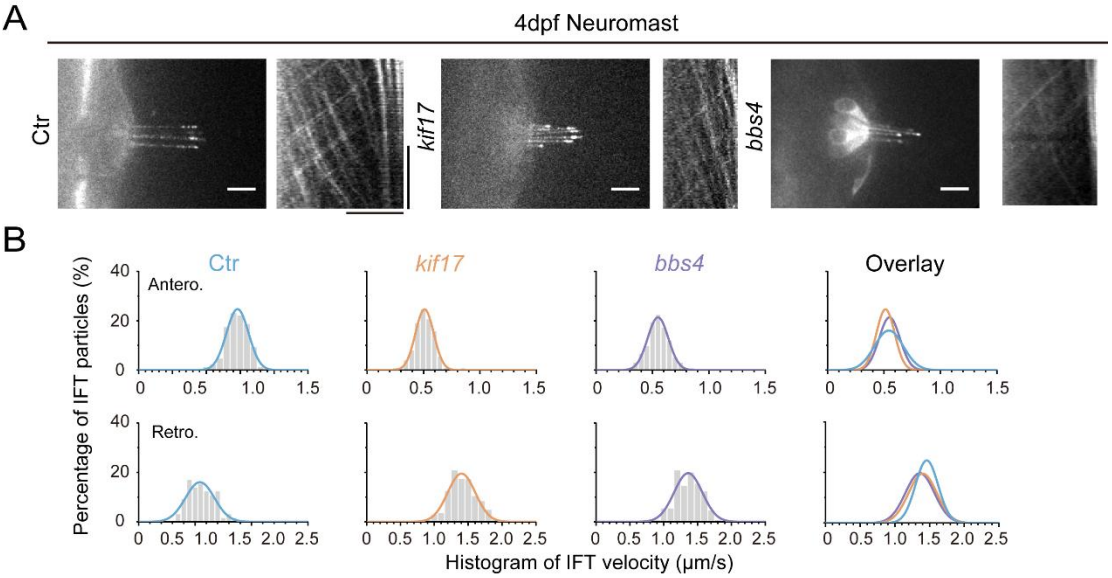

Figure S3 IFT in the cilia of neuromast hair cells of different zebrafish mutants.

(A)(Left) Snapshot of IFT videos in neuromast cilia of 4dpf control, *kif17* or *bbs4* mutants. (Right) Kymographs showing IFT particle movement along axoneme.(B) Histograms showing anterograde and retrograde IFT velocity in neuromast cilia in control and mutants. Horizontal scale bar=10μm. Vertical scale bar=10s

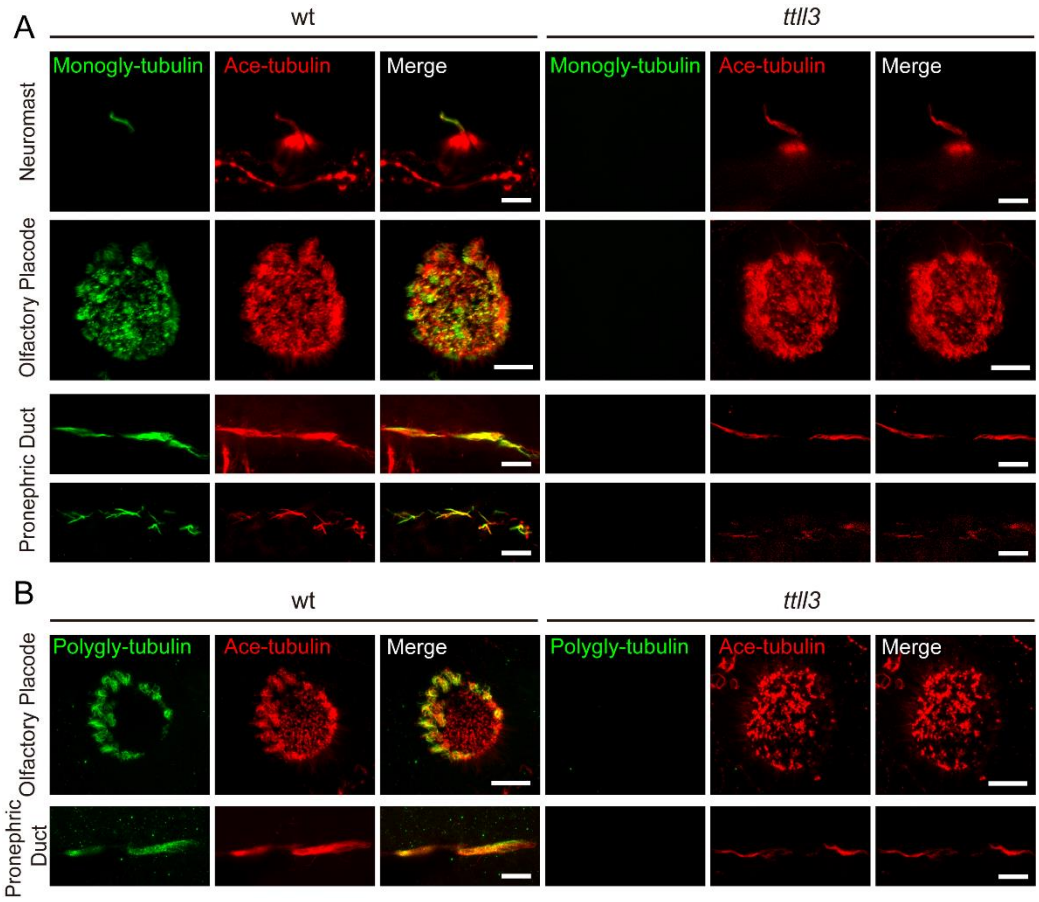

Figure S4 Complete loss of tubulin glycylation in *ttll3* mutants.

(A) Immunostaining with anti-monoglycylated tubulin antibody in 4dpf *ttll3* mutants showing complete absence of monoglycylation modification in cilia of neuromast, olfactory placode and pronephric duct. (B) Immunostaining with anti-polyglycylated tubulin antibody revealed complete elimination of polyglycylation modification in multicilia of olfactory placode and pronephric duct. Red channel shows cilia visualized with anti-acetylated α-tubulin antibody. Scale bar=5 μm.

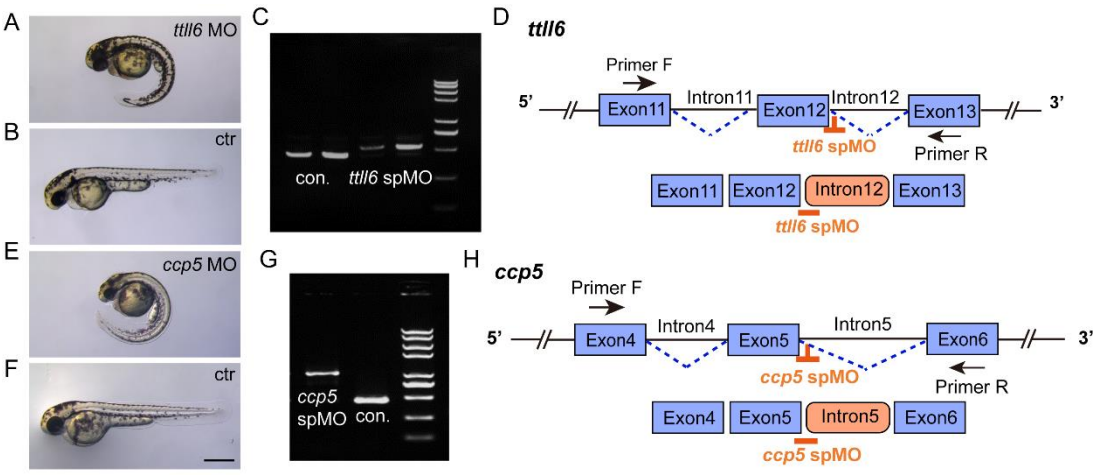

Figure S5 Validation of the efficiency of *ttll6* and *ccp5* morpholinos.

(A, B, E ,F) External phenotypes of control, *ttll6* and *ccp5* morphant embryos at 2 dpf. (C) Agarose gel electrophoresis of RT-PCR amplicons using primer pairs as indicated in panel (D). The PCR product size in the *ttll6* morphants was significantly larger than that in the control (con.). (D) Schematic diagram of *ttll6* sp MO target sites (orange) and RT-PCR primer positions. Sequencing results indicated that *ttll6* morphant exhibited incorrect splicing, with intron12 being wrongly included in the mature mRNA.(G) Agarose gel analysis of RT-PCR amplicons using primer pairs as indicated in panel (H). The PCR product size in the *ccp5* morphant was significantly larger than that in the control (con.). (H)Schematic diagram illustrating the splice donor sites targeted by antisense morpholinos (orange). Injection of *ccp5* MO resulted in the production of aberrant transcripts, wherein intron 5 was mis-spliced into the mature mRNA. Scale bar =500 μm.

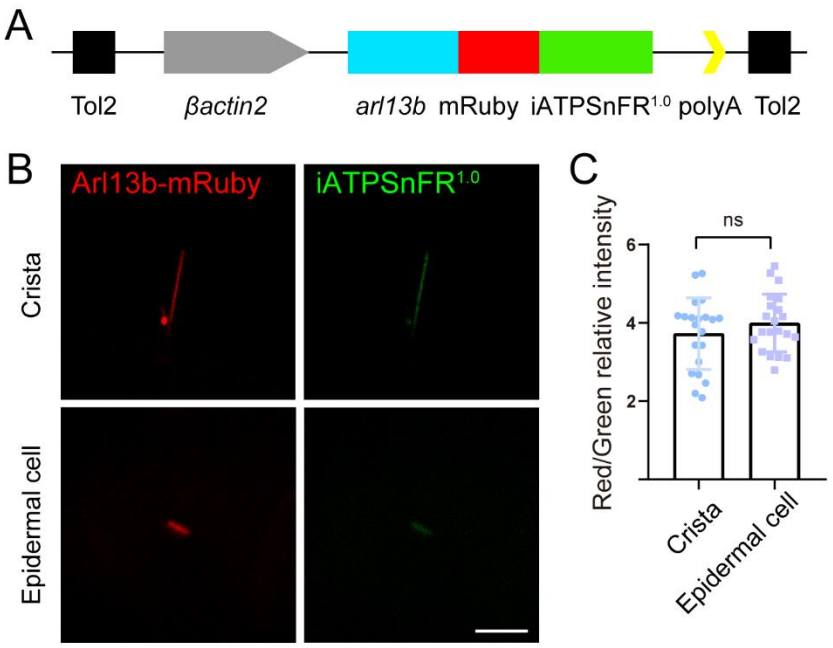

Figure S6 Generation of ATP reporter transgenic line.

(A) Schematic diagram of *βactin2: arl13b-mRuby-iATPSnFR1.0* transgenic construct. (B) Confocal images showing cilia of crista and epidermal cell in 4dpf transgenic embryos. (C) Statistical results of relative fluorescence intensity in cilia of crista and epicell cells (ratio of red fluorescence intensity vs green fluorescence intensity).

Table S1

IFT average velocities in ear crista cilia of control or mutant larvae. (mean ± s.d.,μm/s)

	Anterograde	Retrograde
ctr	0.65±0.10(182)	1.58±0.21(168)
kif3b	0.73±0.09(116)	1.74±0.22(97)
kif17	0.60±0.08(128)	1.72±0.18(137)
bbs4	0.61±0.08(111)	1.49±0.19(126)

IFT average velocities in neuromast cilia of control or mutant larvae. (mean ± s.d.,μm/s)

	Anterograde	Retrograde
ctr	0.56±0.12(66)	1.46±0.15(87)
kif17	0.52±0.08(127)	1.42±0.20(145)
bbs4	0.55±0.09(135)	1.36±0.19(131)

IFT average velocities in larvae injected ctr MO, *ccp5* MO and *ttll6* MO.(mean ± s.d.,μm/s)

	Anterograde	Retrograde
ctr MO	0.56±0.09(288)	1.51±0.20(257)
ccp5 MO	0.63±0.10(257)	1.56±0.23(235)
ttll6 MO	0.52±0.09(306)	1.38±0.18(306)

IFT average velocities in crista cilia of control and *ttll3* mutant larvae. (mean ± s.d.,μm/s)

	Anterograde	Retrograde
ctr	0.71±0.10(490)	1.57±0.19(550)
ttll3	0.69±0.09(482)	1.56±0.18(554)

Table S1 Summary of IFT average velocities in different zebrafish muants or morphants.

Supplementary Videos

Time-lapse images were continuously collected at an exposure time of 200 ms. The display rate was 20 frames per second. Scale bar: 10 μm.

Video 1： Fluorescence time-lapse movie of ear crista cilia visualized by *Tg(hsp70l: ift88-GFP)*.

Video 2： Fluorescence time-lapse movie of neuromast cilia visualized by *Tg(hsp70l: ift88-GFP)*.

Video 3： Fluorescence time-lapse movie of pronephric duct cilia visualized by *Tg(hsp70l: ift88-GFP)*.

Video 4： Fluorescence time-lapse movie of spinal cord cilia visualized by *Tg(hsp70l: ift88-GFP).*

Video 5： Fluorescence time-lapse movie of skin epidermal cells cilia visualized by *Tg(hsp70l: ift88-GFP).*

Video 6-9： Fluorescence time-lapse movies of ear crista cilia in *kif17*, *kif3b*, *bbs4* and *ttll3* mutants visualized by *Tg(hsp70l: ift88-GFP)*.

Video 10： Fluorescence time-lapse movies of ear crista cilia in *Tg(hsp70l: ift88-GFP)* embryos injected with lower dose of *ift88* morpholinos.

REFERENCES

Berbari, N.F., Lewis, J.S., Bishop, G.A., Askwith, C.C., and Mykytyn, K. (2008). Bardet-Biedl syndrome proteins are required for the localization of G protein-coupled receptors to primary cilia. Proc Natl Acad Sci U S A *105*, 4242-4246.

Bhogaraju, S., Cajanek, L., Fort, C., Blisnick, T., Weber, K., Taschner, M., Mizuno, N., Lamla, S., Bastin, P., Nigg, E.A*., et al.* (2013). Molecular basis of tubulin transport within the cilium by IFT74 and IFT81. Science *341*, 1009-1012.

Chan, Y.H., and Marshall, W.F. (2012). How cells know the size of their organelles. Science *337*, 1186-1189.

Engel, B.D., Ludington, W.B., and Marshall, W.F. (2009). Intraflagellar transport particle size scales inversely with flagellar length: revisiting the balance-point length control model. J Cell Biol *187*, 81-89.

Gadadhar, S., Alvarez Viar, G., Hansen, J.N., Gong, A., Kostarev, A., Ialy-Radio, C., Leboucher, S., Whitfield, M., Ziyyat, A., Toure, A*., et al.* (2021). Tubulin glycylation controls axonemal dynein activity, flagellar beat, and male fertility. Science *371*.

Goetz, S.C., and Anderson, K.V. (2010). The primary cilium: a signalling centre during vertebrate development. Nat Rev Genet *11*, 331-344.

Hesketh, S.J., Mukhopadhyay, A.G., Nakamura, D., Toropova, K., and Roberts, A.J. (2022). IFT-A structure reveals carriages for membrane protein transport into cilia. Cell *185*, 4971-4985 e4916.

Hong, S.R., Wang, C.L., Huang, Y.S., Chang, Y.C., Chang, Y.C., Pusapati, G.V., Lin, C.Y., Hsu, N., Cheng, H.C., Chiang, Y.C*., et al.* (2018). Spatiotemporal manipulation of ciliary glutamylation reveals its roles in intraciliary trafficking and Hedgehog signaling. Nat Commun *9*, 1732.

Ishikawa, H., Moore, J., Diener, D.R., Delling, M., and Marshall, W.F. (2023). Testing the ion-current model for flagellar length sensing and IFT regulation. Elife *12*.

Janke, C., and Bulinski, J.C. (2011). Post-translational regulation of the microtubule cytoskeleton: mechanisms and functions. Nat Rev Mol Cell Biol *12*, 773-786.

Jin, H., White, S.R., Shida, T., Schulz, S., Aguiar, M., Gygi, S.P., Bazan, J.F., and Nachury, M.V. (2010). The conserved Bardet-Biedl syndrome proteins assemble a coat that traffics membrane proteins to cilia. Cell *141*, 1208-1219.

Jordan, M.A., Diener, D.R., Stepanek, L., and Pigino, G. (2018). The cryo-EM structure of intraflagellar transport trains reveals how dynein is inactivated to ensure unidirectional anterograde movement in cilia. Nat Cell Biol *20*, 1250-1255.

Kardon, J.R., and Vale, R.D. (2009). Regulators of the cytoplasmic dynein motor. Nature Reviews Molecular Cell Biology *10*, 854.

Kozminski, K.G., Beech, P.L., and Rosenbaum, J.L. (1995). The Chlamydomonas kinesin-like protein FLA10 is involved in motility associated with the flagellar membrane. J Cell Biol *131*, 1517-1527.

Kozminski, K.G., Johnson, K.A., Forscher, P., and Rosenbaum, J.L. (1993). A motility in the eukaryotic flagellum unrelated to flagellar beating. Proceedings of the National Academy of Sciences *90*, 5519-5523.

Kwan, K.M., Fujimoto, E., Grabher, C., Mangum, B.D., Hardy, M.E., Campbell, D.S., Parant, J.M., Yost, H.J., Kanki, J.P., and Chien, C.B. (2007). The Tol2kit: A multisite gateway-based construction kit for Tol2 transposon transgenesis constructs. Developmental Dynamics.

Lechtreck, K.F., Johnson, E.C., Sakai, T., Cochran, D., Ballif, B.A., Rush, J., Pazour, G.J., Ikebe, M., and Witman, G.B. (2009). The Chlamydomonas reinhardtii BBSome is an IFT cargo required for export of specific signaling proteins from flagella. J Cell Biol *187*, 1117-1132.

Liu, Y.X., Xue, B., Sun, W.Y., Wingfield, J.L., Sun, J., Wu, M., Lechtreck, K.F., Wu, Z., and Fan, Z.C. (2021). Bardet-Biedl syndrome 3 protein promotes ciliary exit of the signaling protein phospholipase D via the BBSome. Elife *10*.

Lobas, M.A., Tao, R., Nagai, J., Kronschlager, M.T., Borden, P.M., Marvin, J.S., Looger, L.L., and Khakh, B.S. (2019). A genetically encoded single-wavelength sensor for imaging cytosolic and cell surface ATP. Nat Commun *10*, 711.

Ludington, W.B., Wemmer, K.A., Lechtreck, K.F., Witman, G.B., and Marshall, W.F. (2013). Avalanche-like behavior in ciliary import. Proc Natl Acad Sci U S A *110*, 3925-3930.

Marshall, W.F. (2023). The flagellar length control system: exploring the physical biology of organelle size. Phys Biol *20*.

Meleppattu, S., Zhou, H., Dai, J., Gui, M., and Brown, A. (2022). Mechanism of IFT-A polymerization into trains for ciliary transport. Cell *185*, 4986-4998 e4912.

Mill, P., Christensen, S.T., and Pedersen, L.B. (2023). Primary cilia as dynamic and diverse signalling hubs in development and disease. Nat Rev Genet *24*, 421-441.

Nachury, M.V., Loktev, A.V., Zhang, Q., Westlake, C.J., Peranen, J., Merdes, A., Slusarski, D.C., Scheller, R.H., Bazan, J.F., Sheffield, V.C.*, et al.* (2007). A core complex of BBS proteins cooperates with the GTPase Rab8 to promote ciliary membrane biogenesis. Cell *129*, 1201-1213.

Nachury, M.V., and Mick, D.U. (2019). Establishing and regulating the composition of cilia for signal transduction. Nat Rev Mol Cell Biol *20*, 389-405.

O'Hagan, R., Silva, M., Nguyen, K.C.Q., Zhang, W., Bellotti, S., Ramadan, Y.H., Hall, D.H., and Barr, M.M. (2017). Glutamylation Regulates Transport, Specializes Function, and Sculpts the Structure of Cilia. Curr Biol *27*, 3430-3441 e3436.

Ogino, T., Sawada, M., Takase, H., Nakai, C., Herranz-Pérez, V., Cebrián-Silla, A., Kaneko, N., García-Verdugo, J.M., and Sawamoto, K. (2016). Characterization of multiciliated ependymal cells that emerge in the neurogenic niche of the aged zebrafish brain. Journal of Comparative Neurology *524*, 2982-2992.

Orozco, J.T., Wedaman, K.P., Signor, D., Brown, H., Rose, L., and Scholey, J.M. (1999). Movement of motor and cargo along cilia. Nature *398*, 674.

Ou, G., Blacque, O.E., Snow, J.J., Leroux, M.R., and Scholey, J.M. (2005). Functional coordination of intraflagellar transport motors. Nature *436*, 583-587.

Ou, G., Koga, M., Blacque, O.E., Murayama, T., Ohshima, Y., Schafer, J.C., Li, C., Yoder, B.K., Leroux, M.R., and Scholey, J.M. (2007). Sensory ciliogenesis in Caenorhabditis elegans: assignment of IFT components into distinct modules based on transport and phenotypic profiles. Mol Biol Cell *18*, 1554-1569.

Pathak, N., Austin-Tse, C.A., Liu, Y., Vasilyev, A., and Drummond, I.A. (2014). Cytoplasmic carboxypeptidase 5 regulates tubulin glutamylation and zebrafish cilia formation and function. Mol Biol Cell *25*, 1836-1844.

Pathak, N., Austin, C.A., and Drummond, I.A. (2011). Tubulin tyrosine ligase-like genes ttll3 and ttll6 maintain zebrafish cilia structure and motility. J Biol Chem *286*, 11685-11695.

Reiter, J.F., and Leroux, M.R. (2017). Genes and molecular pathways underpinning ciliopathies. Nat Rev Mol Cell Biol *18*, 533-547.

Rosenbaum, J.L., Moulder, J.E., and Ringo, D.L. (1969). Flagellar elongation and shortening in Chlamydomonas. The use of cycloheximide and colchicine to study the synthesis and assembly of flagellar proteins. J Cell Biol *41*, 600-619.

Scholey, and J., M. (2008). Intraflagellar transport motors in cilia: moving along the cell's antenna. The

Journal of Cell Biology *180*, 23-29.
Singla, V., and Reiter, J.F. (2006). The primary cilium as the cell's antenna: signaling at a sensory organelle. Science *313*, 629-633.
Sirajuddin, M., Rice, L.M., and Vale, R.D. (2014). Regulation of microtubule motors by tubulin isotypes and post-translational modifications. Nat Cell Biol *16*, 335-344.
Snow, J.J., Ou, G., Gunnarson, A.L., Walker, M.R., Zhou, H.M., Brust-Mascher, I., and Scholey, J.M. (2004). Two anterograde intraflagellar transport motors cooperate to build sensory cilia on C. elegans neurons. Nat Cell Biol *6*, 1109-1113.
Song, Z., Zhang, X., Jia, S., Yelick, P.C., and Zhao, C. (2016). Zebrafish as a Model for Human Ciliopathies. Journal of Genetics & Genomics *43*, 107-120.
Stepanek, L., and Pigino, G. (2016). Microtubule doublets are double-track railways for intraflagellar transport trains. Science *352*, 721-724.
Stukalin, E.B., Phillips, H., 3rd, and Kolomeisky, A.B. (2005). Coupling of two motor proteins: a new motor can move faster. Phys Rev Lett *94*, 238101.
Taschner, M., Bhogaraju, S., and Lorentzen, E. (2012). Architecture and function of IFT complex proteins in ciliogenesis. Differentiation *83*, S12-S22.
Tsujikawa, M., and Malicki, J. (2004). Intraflagellar Transport Genes Are Essential for Differentiation and Survival of Vertebrate Sensory Neurons. Neuron *42*, 703-716.
Urnavicius, L., Lau, C.K., Elshenawy, M.M., Morales-Rios, E., Motz, C., Yildiz, A., and Carter, A.P. (2018). Cryo-EM shows how dynactin recruits two dyneins for faster movement. Nature *554*, 202-206.
Vannuccini, E., Paccagnini, E., Cantele, F., Gentile, M., Dini, D., Fino, F., Diener, D., Mencarelli, C., and Lupetti, P. (2016). Two classes of short intraflagellar transport train with different 3D structures are present in Chlamydomonas flagella. J Cell Sci *129*, 2064-2074.
Visscher, K., Schnitzer, M.J., and Block, S.M. (1999). Single kinesin molecules studied with a molecular force clamp. Nature *400*, 184-189.
Wemmer, K., Ludington, W., and Marshall, W.F. (2020). Testing the role of intraflagellar transport in flagellar length control using length-altering mutants of Chlamydomonas. Philos Trans R Soc Lond B Biol Sci *375*, 20190159.
Wloga, D., Webster, D.M., Rogowski, K., Bre, M.H., Levilliers, N., Jerka-Dziadosz, M., Janke, C., Dougan, S.T., and Gaertig, J. (2009). TTLL3 Is a tubulin glycine ligase that regulates the assembly of cilia. Dev Cell *16*, 867-876.
Ye, F., Nager, A.R., and Nachury, M.V. (2018). BBSome trains remove activated GPCRs from cilia by enabling passage through the transition zone. J Cell Biol *217*, 1847-1868.
Zhao, C., Omori, Y., Brodowska, K., Kovach, P., and Malicki, J. (2012). Kinesin-2 family in vertebrate ciliogenesis. Proceedings of the National Academy of Sciences *109*, 2388 - 2393.